A Free-Flooding Acoustical Resonator for Measurement of Bubble Size Distributions

DAVID M. FARMER AND SVEIN VAGLE

Institute of Ocean Sciences, Sidney, British Columbia, Canada

A. DONALD BOOTH

Autonetics Research, Sooke, British Columbia, Canada

(Manuscript received 28 January 1997, in final form 11 October 1997)

ABSTRACT

An instrument for the measurement of bubble size distributions is described. The sensing element exploits the free-flooding resonator design of Medwin with modifications to overcome the limitations in the original implementation, especially those due to a sensitivity to ambient pressure fluctuations in the surrounding medium. A mathematical model of the resonator provides insight into the factors affecting its performance and motivates application of appropriate signal processing algorithms. Comparison of different bubble size calculation methods shows the direct approach of Commander and MacDonald to be most successful. The stability of this new implementation of the resonator facilitates accurate measurement of the complex dispersion relation. Comparison of the real and imaginary components then leads to the definition of a measurement quality factor that may be calculated for each sample. Practical considerations are discussed for implementation of autonomous battery-powered resonator arrays for ocean deployments with real-time data processing. Examples are presented of measured bubble size distributions acquired from an autonomous array of five instruments moored in the Gulf of Mexico.

1. Introduction

Bubble populations play a role in many aspects of oceanography, including the flux of momentum and gas across the air–sea interface, acoustical and electromagnetic properties of the ocean surface layer, the formation of atmospheric particulates, and certain biological and biochemical effects. The scattering properties of bubbles are also used in acoustical measurement of ocean surface layer dynamics. Calculation of the contributions of bubbles to these phenomena requires knowledge of their size distribution. This need has motivated development of a variety of optical and acoustical techniques. A diverse approach to the measurement task is almost certainly required since the enormous range of natural bubble populations appears to preclude use of any single technique for all distributions. In this paper we explore a new implementation of the acoustical resonator concept described by Medwin and Breitz (1989). In addition to providing a theoretical analysis of its operation, we show how it may be used to measure the complex dispersion of the bubbles over a wide frequency range, leading to a check on the consistency of the measurement. The present design provides immunity to pressure sensitivity and allows autonomous operation; its performance is illustrated with data acquired in the open ocean.

Previous approaches to the measurement of oceanic bubble size distributions include the use of bubble traps (Blanchard and Woodcock 1957; Kolovayev 1976) and the photographic techniques of Johnson and Cooke (1979), Walsh and Mulhearn (1987), and others. Acoustical techniques for bubble measurement were pioneered by Medwin and his students, who investigated a variety of techniques based on the linear acoustical behavior of bubbles (Medwin 1970, 1977a,b,c), in addition to the resonator concept discussed here (Medwin and Breitz 1989; Breitz and Medwin 1989). A related approach involving the application of multiple-frequency travel time sonar has been discussed by Lamarre (1993), Melville et al. (1995), and Vagle and Farmer (1998). Nonlinear acoustical methods have also been developed (Newhouse and Shankar 1984; Akulichev and Bulanov 1987; Leighton et al. 1991, 1992; Phelps and Leighton 1996). All of these approaches involve in situ measurement requiring an instrument to be deployed in the water being sampled. Thorpe (1982, 1983) first demonstrated the power of acoustical remote sensing using backscatter sonar in this context, although interpretation of a single-frequency measurement depends on assumptions about the bubble size distribution. This ap-

Corresponding author address: Dr. David M. Farmer, Institute of Ocean Sciences, 9860 W. Saanich Road, Sidney, BC V8L 4B2, Canada.
E-mail: farmerd@dfo-mpo.gc.ca

proach has been extended to multiple-frequency sonar by Vagle and Farmer (1992) and Szczucka (1989) to recover bubble size distributions.

Ocean observations have led to a large range of measured bubble size distributions. Much of this variability must be ascribed to the physical environment, but uncertainty in instrument performance and analytical procedures remains. These considerations motivate the present effort. We have focused on the resonator design because of its potential for accurate and instantaneous measurement with fine resolution over a wide range of acoustical frequencies. As will be shown subsequently, this characteristic, coupled with the ability to measure both real and imaginary components of the dispersion relation, makes possible a useful internal check on the measurement quality.

2. Measurement of complex sound speed with a resonator

The resonant cavity is bounded by two reflecting disks but is otherwise open, allowing free movement of water through the measurement volume. The instrument mooring is typically fitted with a vane and deployed in such a way as to tend to point into the current, thus minimizing the possibility of flow interference. The essential idea is that a broadband acoustical field is generated within the cavity producing a large number of resonant modes that are detected by hydrophone. In Medwin's original design (Medwin and Breitz 1989; Breitz and Medwin 1989), sound transmission into the cavity is achieved with a charged, coated Mylar sheet (Fig. 1a), while a hydrophone inserted within the opposing disk is used to detect the acoustical field. Bubbles in the intervening medium extract energy through the usual damping mechanisms, thus attenuating the resonant peaks. The degree of damping was measured from the change in peak height or width, thus providing a basis for deriving the bubble population.

The speed of sound in a compressible continuum is given by the bulk modulus $B = -V(dp/dV)$, where V is the ambient volume, dp is change in pressure, and dV is change in volume, such that the speed of sound is given by $c = (B/\rho)^{1/2}$, where ρ is the water density. The complex dispersion relationship in a bubbly mixture is given by Leighton (1994):

$$\frac{c_0^2}{c_m^2} = 1 + 4\pi c_0^2 \int_0^\infty \frac{aN(a)}{\omega_0^2 - \omega^2 + i\delta\omega^2}\, da, \qquad (1)$$

where c_0 is the speed of sound in pure liquid, c_m is the complex sound speed in the fluid with bubbles, a is the bubble radius, ω is the measurement frequency, ω_0 is the natural frequency of a bubble of radius a, δ is the bubble damping that is defined later in (15) and (16) and is a function of both bubble radius a and acoustical frequency ω, and $N(a)$ is the bubble density function within a 1-μm radius range da centered at a. Solving (1) to determine $N(a)$ depends on contributions from bubbles of all sizes within the measurement volume. Since the resonance quality factor Q of a bubble in freshwater is typically rather high [7–23 for bubble radii between 15 and 550 μm, respectively, although possibly somewhat less in seawater (A. R. Kolaini 1997, personal communication)], the dependence of complex sound speed on contributions from bubbles far from resonance is reduced. However, the full spectrum must be considered and, in general, a simple ''zero order'' calculation based on the local peak height is inadequate. We have carried out inversions in which Q has been reduced by a factor of 2 with respect to the freshwater values. These show insignificant changes to the bubble size distributions, with modest reductions in estimated densities at the largest bubble radii but negligible effects for bubble radii less than 200 μm.

A given bubble size distribution results in modification of both real and imaginary components of the sound speed. An element of the technique discussed here

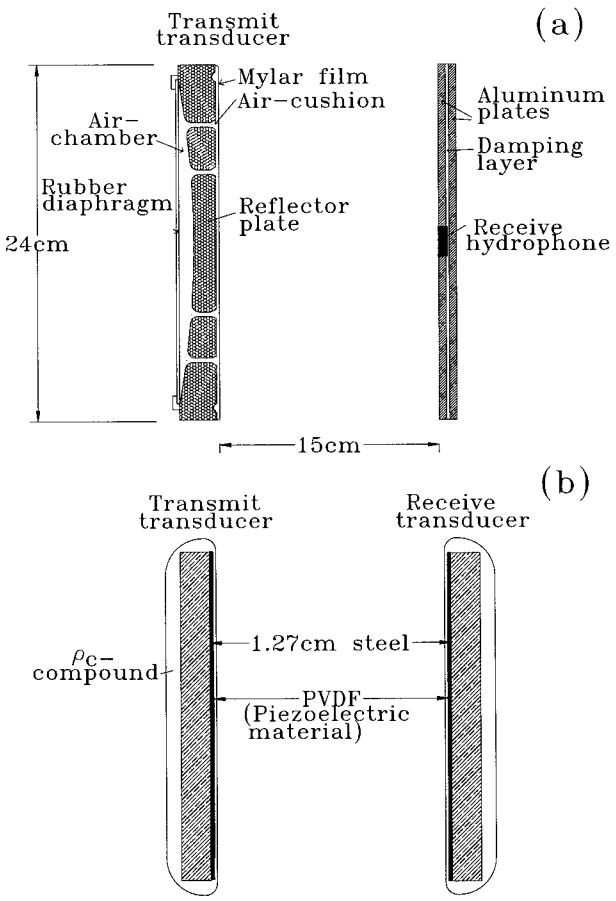

FIG. 1. Side view of two resonator designs: (a) an early version of Medwin's design (after Buxcey et al. 1965) with transmitter on left and hydrophone on right. The transmitter uses an air-backed, coated Mylar film. (b) New design with identical PVDF-covered reflector plates for transmission and detection. Both plates are circular.

is the application of both components to verify internal consistency of the measurement.

3. Resonator design

It is clear that the basic concept put forward by Breitz and Medwin (1989) offers many advantages, not least of which is the large number of resonator harmonics that can be used to derive bubble spectra with high resolution. However, the original design, which has been followed in subsequent implementations and compared to optical data in laboratory experiments (Su et al. 1994), suffers from certain shortcomings; these became apparent to us when we built a duplicate instrument following the published design. Figure 1a shows an early implementation described by Buxcey et al. (1965). Although the design details may vary to some extent, the basic technique for transmitting sound into the cavity is by use of a charged, air-backed, coated Mylar sheet. The air space may be very small, consisting, for example, of small gaps around natural roughness elements or artificial scoring on the backing plate surface, but is nevertheless essential, since Mylar is not itself a piezoelectric material but instead transmits sound through its motion when driven by a modulated electric potential relative to an adjacent electrode.

As may readily be demonstrated by experiment, some form of pressure equalization is required since the spacing between the Mylar and the backing plate determines the sensitivity of the instrument. For example, Buxcey et al. (1965) describe the way in which the backing plate may be grooved with a series of channels connected to a pressure-equalizing chamber at the rear. Alternative implementations allow for a single port to a small rubber diaphragm. Although these and similar arrangements allow for an average hydrostatic compensation, they are insufficient for accurate ocean measurements. For observations in the active near surface of the ocean, any flow past the sensor will produce a dynamic pressure head across the plate that can never be fully compensated with a passive mechanism such as a diaphragm. Tests with various coated Mylar transducers confirmed the problems of pressure sensitivity, some of which had been noted previously by Buxcey et al. (1965) and Medwin (1996, personal communication). The tests also identified a lack of consistency in Mylar resonator performance.

Signal detection on the Medwin resonator is achieved with a small hydrophone embedded in the reflector plate. Some sensitivity to the location can occur due to reflections from the supporting frame, and variations in transmission efficiency of the Mylar at different locations on the transmitting plate can occur for the reasons noted above.

These considerations motivated a modification of Medwin's original design. We used two identical steel plates (as shown in Fig. 1b), each covered with a layer of PVDF (polyvinylidenedifluoride) piezoelectric material (piezoelectric ceramic may also be used). The steel plate and PVDF transducer is covered with ρc compound. Although the steel plates have sharp edges, the ρc compound may be shaped so as to minimize flow separation effects that could otherwise lead to concerns about inhomogeneity of bubble transport. We also emphasize here that the resonator mooring is oriented with a vane so that the predominant orbital motion is orthogonal to the resonator axis.

One of these piezoelectric films is used to generate broadband noise; the other serves as a hydrophone. The performance of PVDF is essentially independent of pressure over the modest depths considered here. It is thin relative to an acoustic wavelength and has an impedance close to that of water, resulting in negligible contribution to the reflection boundary conditions. Besides serving as a pressure-insensitive sound source, the PVDF also acts as a distributed hydrophone over the entire face of the opposing plate; this arrangement limits effects of scatter from the plate spacer bars. A number of other differences in design, operation, and signal processing have been introduced as a result of analysis of instrument operation and of field and laboratory tests of its performance.

4. Theory of a free-flooding acoustic resonator

In the present design the resonator has two identical reflecting plates (Fig. 1b). Before discussing the problem of multiple reflection between the opposing sides of the cavity, we note that acoustic reflection from a single plate was first analyzed by the mathematician George Green (1838). The reflectivity of a sound wave at angular frequency ω by a plate of thickness d of material with density ρ and sound speed c immersed in a fluid with parameters ρ_1 and c_1 is

$$R = \frac{\left(\frac{\rho c}{\rho_1 c_1} - \frac{\rho_1 c_1}{\rho c}\right)}{\sqrt{4\cot^2\left(\frac{\omega d}{c_1}\right) + \left(\frac{\rho c}{\rho_1 c_1} + \frac{\rho_1 c_1}{\rho c}\right)^2}}. \quad (2)$$

The corresponding phase shift ε referred to the surface of the plate is

$$\varepsilon = \frac{\pi}{2} - \arctan\left[\frac{1}{2}\left(\frac{\rho c}{\rho_1 c_1} + \frac{\rho_1 c_1}{\rho c}\right)\tan\left(\frac{\omega d}{c_1}\right)\right]. \quad (3)$$

Figure 2 shows the reflectivity calculated from (2) as a function of frequency for different plate thickness and materials. Nulls occur at higher frequencies due to interference with reflection from the back of the plate. Selection of plate thickness and material is based on the requirement for high reflectivity and avoidance of interference. (More complex plate designs using a sandwich construction, as in Fig. 1a, can minimize back reflection but will not be discussed further here because,

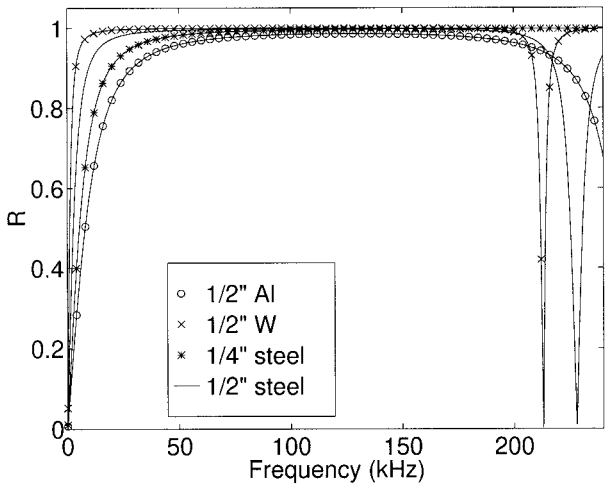

FIG. 2. Reflectivity calculated from (2) for aluminum, tungsten, and steel of different thickness.

as shown in Fig. 2, for the materials and plate thickness used, reflection from the back of the plate is not a problem within the frequency range of interest.) To achieve high reflectivity, the numerator of (2) must be maximized. Although depleted uranium or drawn tungsten would be good choices, cost dictates the use of steel as a reasonable compromise.

The Fresnel–Huygens formula for the transient signal following excitation of a circular transmitter in piston mode (Fig. 3) is

$$p_R = \frac{ik}{4\pi}\int_A p_0 \frac{\exp(-ikX)}{X}(1 + \cos\theta)\, dS, \qquad (4)$$

where p_R is the field at vector position X from the center of the transmitting disk, θ is the angle that this vector makes with the normal to the disk, λ is the acoustic wavelength, $k = 2\pi/\lambda$, and the surface integral is taken over the whole area of the transmitter. The term $(1 + \cos\theta)$ is included to approximate the Green's function in the near field.

In our case, the field is radially symmetric about the z axis, and the above formula becomes

$$p(x, \phi) = \frac{ik}{2\pi}\int_{r=0}^{X}\int_{\theta=0}^{\pi} p_0 \frac{\exp(-ikU)}{U}\left(1 + \frac{z}{U}\right) r\, dr\, d\theta, \qquad (5)$$

where

$$U \equiv (x^2 + z^2 + r^2 - 2rx\cos\theta)^{1/2}. \qquad (6)$$

The term $p(x, \phi)$ is the field vector of sound pressure at vector position x from the center of the transmitter; z is its normal distance from the plane of the transmitter, $k = \omega/c$; and p_0 is the transmitted signal (Fig. 3). Note that while the initial transmitting field p_0 is uniform and has only a real component, the received field is complex with phase ϕ. We model the pressure field between the plates of the resonator by integrating (5) according to the extended Simpson's rule. The adequacy of this approach for the chosen sampling interval was checked in all cases by recalculation with twice as many points, which established that the results were accurate to six decimal places.

Calculation of the field at resonance follows the general method developed by Fox and Li (1961) for analysis of laser cavities. The fundamental assumption is that at resonance the pressure fields on the transmitter and the receiver are identical. If we denote the input pressure field by $p_n(x, \phi)$ and the field produced by it at the reflector by $p_{n+1}(x, \phi)$, after the nth reflection (5) becomes

$$p_{n+1}(x, \phi_{n+1}) = \mathrm{Re}^{i\varepsilon}\frac{ik}{2\pi}\int_{r=0}^{X}\int_{\theta=0}^{\pi} p_n(x, \phi_n)\frac{\exp(-ikU)}{U}\left(1 + \frac{z}{U}\right) r\, dr\, d\theta, \qquad (7)$$

which must be determined numerically and depends upon the complex reflectivity given in (2) and (3). The limit as $n \to \infty$ of the complex ratio P_{n+1}/P_n defines the complex eigenvalue Γ. The exact integral equation (7) is solved for a given frequency and configuration and computes the eigenvalue, power loss, and Q value. The Rayleigh ratio (Booth 1966) is used to improve the eigenvalue estimate when the best eigenvector has been obtained.

As is well known, the assumption that resonances occur when the plate spacing is an exact multiple of the sound wavelength is only approximately true. This makes no difference to the solution of the integral equation as far as the determination of an eigenvalue is concerned. However, a second condition must be met: avoidance of destructive interference requires that the phase distribution of a signal after reflection be identical to that of the original signal at the transmitter. Thus, to investigate the sound field in the region of resonance, it is necessary to add (with phase) all of the signals at the transmitter until equilibrium is reached. The results are shown in Fig. 4, which emphasizes the increasing importance of this correction for lower modes.

A correct application of the resonator measurement to calculation of bubble populations requires analysis of its performance around resonance. The form of the

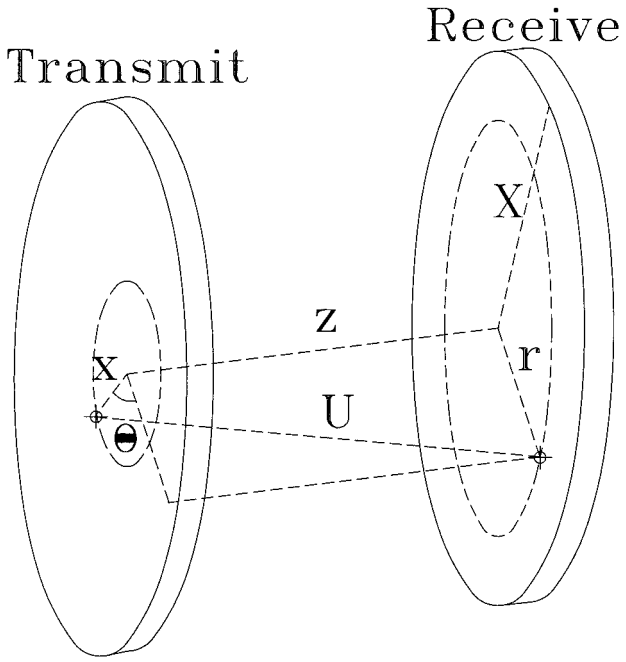

FIG. 3. Coordinate system used in theoretical development.

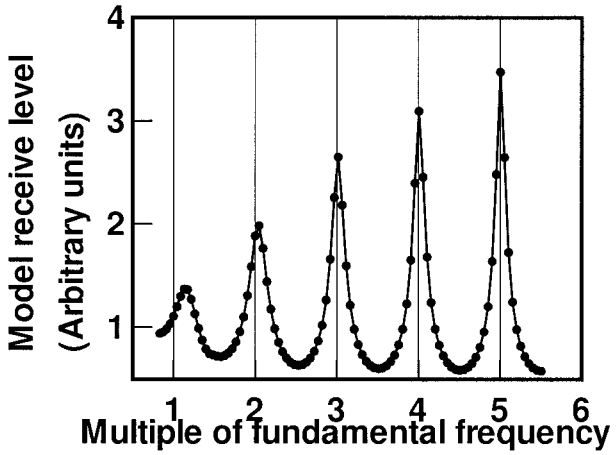

FIG. 4. Model sound pressure field at a plate surface showing the first five modes. Note deviation of lower-mode frequencies from integral sums of nominal fundamental mode frequency.

resonance peaks depends on the signal attenuation on transmission and reflection, that is, the nature of the complex eigenvalue Γ. After M passages between the two reflector plates the total acoustical signal would be

$$A = \sum_{1}^{M} 1 + \Gamma^2 + \Gamma^4 + \cdots + \Gamma^{2M}. \tag{8}$$

We note that the phase difference between corresponding points on the transmitting and receiving plates is constant so that $|\Gamma|$ is evaluated by taking the ratio of signal values at any pair of corresponding points. The associated phase is simply the difference between their phases. Therefore, the summation in (8) becomes

$$|A| = \frac{1}{\sqrt{1 + |\Gamma|^4 - 2|\Gamma|^2 \cos\theta}}, \tag{9}$$

where $\theta = 2(\psi_s - \psi_r)$, and ψ_s and ψ_r are the phases of the transmitted and received signals, respectively. For the fundamental and first harmonic, the resonant frequency, ω_0, is appreciably different from that predicted by simple geometry. At higher modes it is sufficiently accurate to write

$$\theta = 2\frac{z}{c_m}(\omega_0 - \omega). \tag{10}$$

With this assumption, and for $\theta \ll 1$, (9) becomes

$$|A(f)| \approx \frac{1}{\sqrt{(1 - |\Gamma|^2)^2 + 2|\Gamma|^2(2z/c_m)^2(\omega_0 - \omega)^2}}. \tag{11}$$

It is apparent that (11) takes the form of a Lorentzian with peak amplitude $a_p = (1 - |\Gamma|^2)^{-1}$ and resonance quality factor $Q = \sqrt{2}[|\Gamma|(2z/c_m)/(1 - |\Gamma|^2)]$. Figure 5 compares (11) to the model solution for the first mode and shows it to be a good fit, notwithstanding the approximation (10). This result justifies the use of (11) as a functional approximation to measured quantities in the evaluation of peak frequency ω_0 and attenuation.

Having evaluated the resonant frequency for each mode we may solve the integral equation (7) to determine the detailed structure of the respective eigenfunction. As an example, Fig. 6 shows a three-dimensional perspective of the third-mode response. The sensitive volume, represented here by the -6-dB sound pressure level contour, is a variable that depends on resonant mode and is always less than the cylindrical volume enclosed by the two reflecting plates.

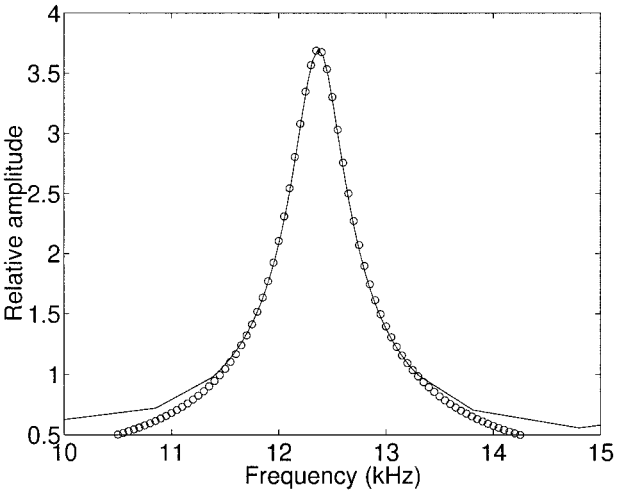

FIG. 5. Least squares fit of (11) to the first harmonic resonator peak. The close fit justifies use of (11) in evaluation of peak properties used in bubble calculations.

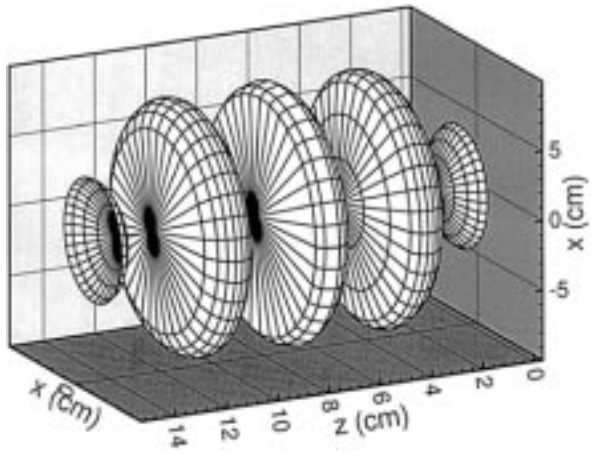

FIG. 6. Three-dimensional perspective view of the mode 3 resonator pressure field 6 dB below maximum. Much of the volume enclosed by the disks is only slightly sensitive to the presence of bubbles.

The bubble distribution may be approximated by a continuous field in which the acoustic properties of the medium are considered homogeneous in space. The influence of bubbles on both real and imaginary components of the sound speed can be obtained from (1) for bubble densities low enough that the fractional term is much less than unity (Leighton 1994):

$$c_{\text{real}} = c_0\left\{1 - (2\pi c_0^2)\int_{a_{\min}}^{a_{\max}} \frac{a}{\omega^2}\,\frac{[(\omega_0/\omega)^2 - 1]N(a)\,da}{\{[(\omega_0/\omega)^2 - 1]^2 + \delta^2\}}\right\} \tag{12}$$

and

$$c_{\text{imag}} = c_{\text{real}}\left\{\int_{a_{\min}}^{a_{\max}} \frac{2\pi a(\omega_0/\omega)^2\delta N(a)\,da}{(\omega_0/c_0)^2\{[(\omega_0/\omega)^2 - 1]^2 + \delta^2\}}\right\}, \tag{13}$$

where $a_{\min}$ and $a_{\max}$ are the bubble radii limits.

Insertion of the complex sound speed into (7) leads to

$$p(x,\,\phi) = \left|\frac{ik}{2\pi}\right| \int_{r=0}^{X}\int_{\theta=0}^{\pi} \frac{p_0}{|\lambda|^2}\,\frac{\exp(-2\pi U\lambda_{\text{imag}})}{U}\left(1 + \frac{z}{U}\right)\left[\sin\left(\frac{2\pi U}{|\lambda|^2}\right)\lambda_{\text{real}} - i\cos\left(\frac{2\pi U}{|\lambda|^2}\right)\lambda_{\text{imag}}\right] r\,dr\,d\theta, \tag{14}$$

where we have used $k = 2\pi/\lambda$ and $\lambda = \lambda_{\text{real}} + \lambda_{\text{imag}}$ in accordance with the use of the complex representation of sound speed in which the real part represents the actual speed of sound through the bubbly medium and the imaginary part represents attenuation of the sound wave by the bubbles.

An example of a model calculation of real and imaginary components for a bubble distribution typical of that measured in the ocean (Fig. 7a) is shown in Figs. 7b,c. The attenuation (Fig. 7b) is large between 10 and 140 kHz, with a maximum at approximately 50 kHz corresponding to a resonant bubble radius of about 65 μm. The corresponding sound speed anomaly (Fig. 7c) illustrates the characteristic change in sign predicted for distributions of bubbles of the same size, although, of course, in this case the details of the shape depend upon the complete bubble size distribution. We note that for this example a zero in the sound speed anomaly occurs at 30 kHz. The fact that the resonator can be used to measure both real and imaginary components of the dispersion relationship allows us to check the internal consistency of the data, to be discussed in section 6.

Laboratory measurements of the sound pressure field were acquired as a function of frequency and position between the plates. In the laboratory a small hydrophone (B&K Type 8103) was mounted so that it could be moved both radially and along the axis between the plates. Measurements were made for the first five modes. Figure 8 shows a sample comparison for the fundamental and third modes. Reasonable agreement is found both in the radial and plate separation components. However, measurement in the narrow antinodes is sensitive to both the precise location and finite dimensions of the hydrophone and support that must also modify the acoustic field within the resonator.

5. Evaluation of bubble size distribution

Recovery of bubble size distributions from measured complex sound speed properties requires knowledge of the physical behavior of bubbles in a sound field. Here we briefly summarize the essential background.

The bubble damping is made up of three components:

$$\delta = \delta_r + \delta_t + \delta_v, \tag{15}$$

where $\delta_r = ka$ represents the damping constant due to radiation, with k being the acoustic wavenumber; $\delta_t = D(\omega_0/\omega)^2$ represents the damping constant due to thermal conductivity; and $\delta_v = 4\mu/(\rho_1\omega a^2)$ is the damping constant due to shear viscosity. Here,

$$\begin{aligned} D &\equiv \frac{3(\gamma - 1)[W\tilde{Y} - 2Z]}{[W^2Z + 3(\gamma - 1)WY]},\\ W &\equiv a(2\omega\rho_g C_p/K)^{1/2},\\ Y &\equiv \sinh W - \sin W,\\ \tilde{Y} &\equiv \sinh W + \sin W,\\ Z &\equiv \cosh W - \cos W, \end{aligned} \tag{16}$$

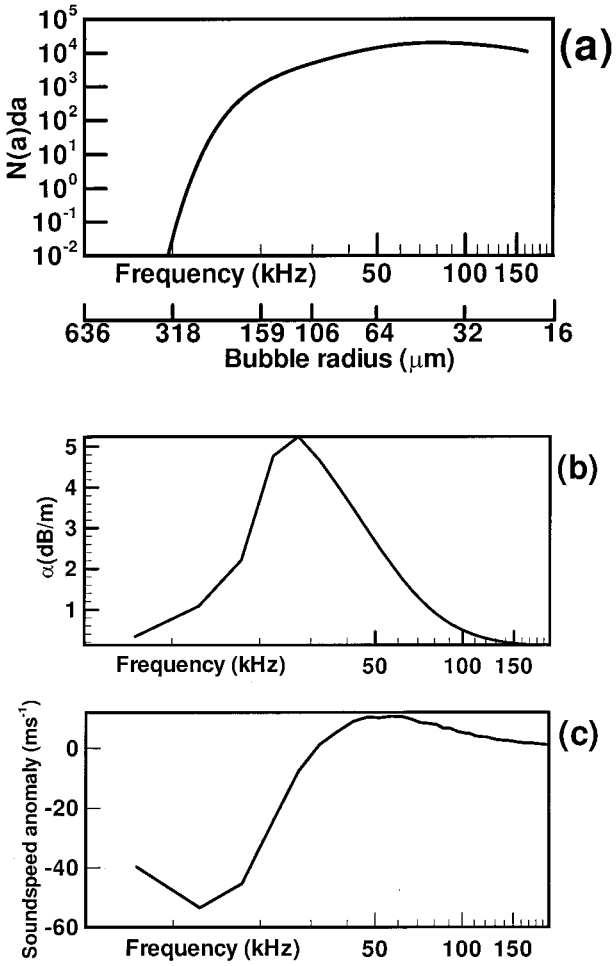

FIG. 7. (a) Typical bubble distribution, (b) model calculation of attenuation, and (c) sound speed anomaly for distribution shown in (a).

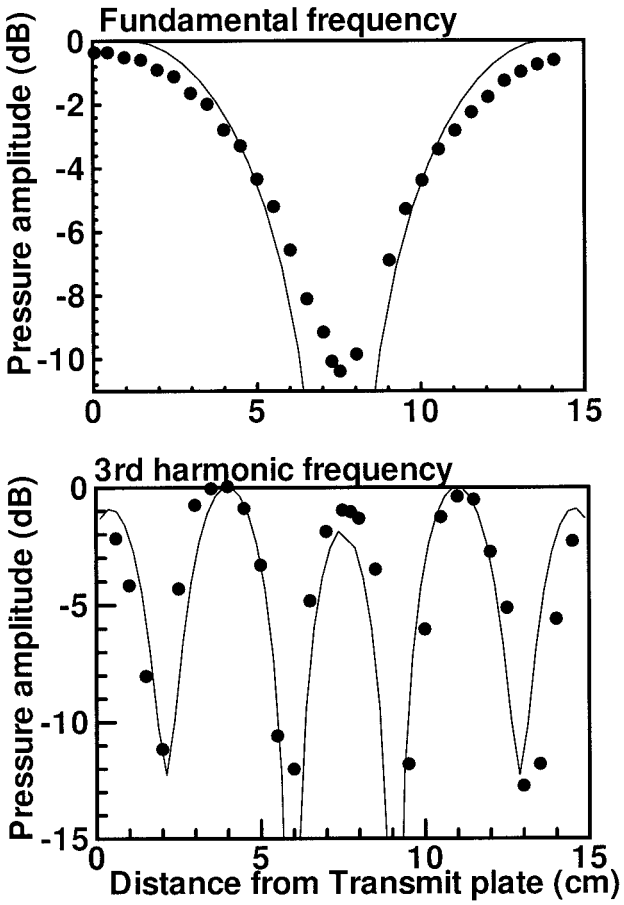

FIG. 8. (a) Comparison with model calculation for the fundamental mode of measured sound pressure level as a function of distance from the transmitter plate along the centerline ($r = 0$). (b) Comparison as in (a) for mode 3.

and τ is the surface tension at the bubble–water interface, P_0 is the ambient pressure, ρ_g is the density of gases in the bubble, K is the thermal conductivity, C_p is the specific heat at constant pressure ($\gamma = C_p/C_v$), and C_v is the specific heat at constant volume.

Morse and Ingard (1968) calculated the temporal pressure wave decay in a cavity after an impulse:

$$p_s(r, t) = \sum_n A_n \exp[-\pi \Delta f_n t] \cos(\omega_n t + \phi_n), \quad (17)$$

or in terms of the squared pressure for each individual mode n as

$$p_n^2 = A_n^2 \exp[-2\pi \Delta f_n t]. \quad (18)$$

Breitz and Medwin (1989) used a simplified representation of the peak shape to estimate the magnitude of the damping term. From linear theory in the steady state, the squared pressure of the nth mode is

$$p_n^2(t) \approx 1/\Delta f_n^2, \quad (19)$$

where Δf_n is the half-power bandwidth of the nth mode.

For a system with small damping, damping factors are additive, and the width of a resonance is proportional to the damping at resonance. On this basis, Breitz and Medwin (1989) obtained the component of resonance width due to bubbles alone (Δf_n^b), as the difference between the width of the nth resonance peak in the bubble-filled water and the corresponding value in the bubble-free water.

Under the assumption that the energy absorbed by the bubbles per unit volume in the cavity is the same as in a traveling wave, the attenuation α per unit distance due to a population $N(a)da$ of bubbles is

$$\alpha(f_n) = -4.3 \int_0^\infty \sigma_e N(a)\, da. \quad (20)$$

Medwin and Breitz (1989) then derive a zeroth-order bubble density function at frequency f_n:

$$N^0(a_n) = 2\pi \Delta f_n^b / c\sigma_e^R 10^6 \delta_R a, \quad (21)$$

where σ_e^R is the resonance value of the extinction cross section and the damping factor δ_R is the applicable value

at resonance. Expression (21) ignores contributions to Δf_n^b from off-resonance bubbles, but higher-order corrections may be made by substituting into (20) an estimated continuous empirical function passing through the points $N^0(a_n)$.

Commander and McDonald (1991) have suggested a different approach. Rather than treat each peak separately and then include a correction term of contributions from other frequencies, they proposed solving (20) directly for the bubble size distribution. They describe a simple finite-element method applying linear cubic splines followed by collocation to generate a system of linear equations for the spline coefficients. The resulting ill-conditioned linear system is solved using singular value decomposition. As shown below (Fig. 9d), a comparison of the two approaches shows that the Breitz and Medwin approximation produces results close to those of Commander and McDonald for bubble radii less than approximately 80 μm but predicts significantly higher densities of larger bubbles. As discussed below, the direct solution of (20) by the method of Commander and McDonald is the most accurate of the two, and this is now used routinely in our resonator data processing. The peak frequency and attenuation are evaluated from a least squares fit of (11) derived above.

Duraiswami (1993) has developed an alternate inversion technique for high signal-to-noise ratios in which both attenuation and phase velocity are used to obtain the bubble size distribution.

6. Data consistency check

Since both real and imaginary components of the dispersion relation over a wide frequency range are measured, we are able to carry out a consistency check on the observations and bubble calculation methods. This approach is illustrated in Fig. 9. Figure 9a shows the resonator peaks, in relative units, measured in bubble-free water. As predicted by the theory, the peak height increases sharply with increasing mode number from the fundamental mode for frequencies below 50 kHz (see Fig. 4). At higher modes it levels off or decreases slightly with increasing frequency, which is in part the consequence of electronic design representing a compromise between transmitted power and power consumption. We note that the highest peaks occur between 30 and 40 kHz, which is also the frequency subject to greatest attenuation by bubbles. Figure 9b shows measurements of the peaks over the lower half of the available frequency range during a 0.3-s sample acquired at 1.9 m at a wind speed of 13 m s^{-1} in the Gulf of Mexico. This sample was chosen to illustrate rather strong attenuation as a bubble cloud passes through the resonator. Note that the peak positions shift relative to the reference peaks acquired in bubble-free water, with peaks below 30 kHz, displaced to lower frequencies and higher frequency peaks displaced to higher frequencies.

The corresponding attenuation is shown in Fig. 9c.

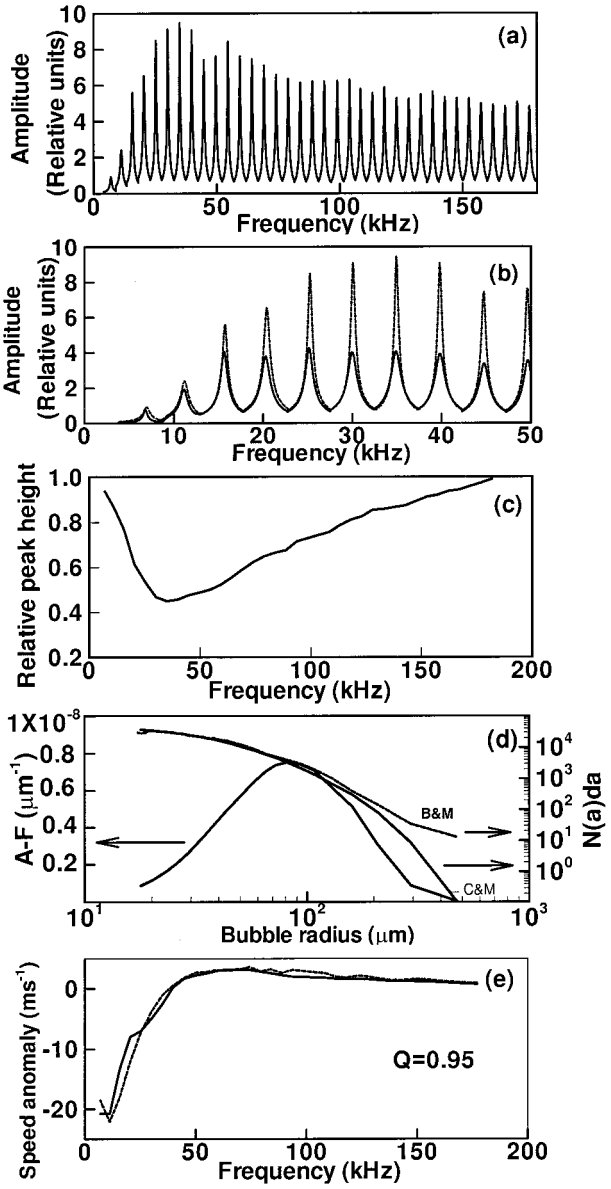

FIG. 9. Sample resonator measurements: (a) Reference spectral peaks without bubbles. (b) Expansion of spectral peaks for the first 10 modes showing measured values with bubbles (solid curve) together with reference peaks (dashed–dotted curve). (c) Measured attenuation of peaks by bubbles. (d) Bubble size distribution derived from attenuation using Commander and McDonald's (C&M) and Breitz and Medwin's (B&M) schemes. The size distribution is also shown as air fraction per unit (μm) radius increment—that is, $N(a)[(4/3)\pi a^3]$. (e) Measured sound speed anomaly (solid curve) and calculated sound speed anomaly (dashed–dotted curve) from attenuation data using (C&M). The measurement quality factor Q_m in this case is 0.950.

Calculations of the bubble size distribution from the attenuation using both the methods of Commander and McDonald (1991) and Breitz and Medwin (1989) are shown in Fig. 9d. An alternative way of expressing the bubble size distribution, which gives a better feel for

the significance of bubble contributions to the total air fraction, is also shown in Fig. 9d, where we have multiplied the number of bubbles at each radius increment by the corresponding volume. It is immediately apparent that the bubble radius contributing most to air fraction is 85 μm (resonant frequency 38 kHz). Finally, in Fig. 9e we show the measured sound speed anomaly derived from the displacements of the spectral peaks in Fig. 9b, together with the inferred sound speed anomaly calculated from the bubble distribution derived from measured attenuation.

Perfect consistency between the measured and calculated sound speed anomalies in Fig. 9e would imply internal consistency between the two quite different measurements of sound speed and attenuation. The discrepancy between these two curves serves as a useful check on data quality. For this purpose we define a measurement quality factor Q_m:

$$Q_m \equiv 1 - \frac{\left| \int |\Delta c(\omega)| \beta(\omega)\, d\omega \right|^2}{\int |dc_{\text{calc}}(\omega)| \beta(\omega)\, d\omega \times \int |dc_{\text{meas}}(\omega)| \beta(\omega)\, d\omega}, \tag{22}$$

where $\beta(\omega)$ is the air fraction at frequency ω, $dc_{\text{cal}}(\omega)$ is the sound speed anomaly calculated from the bubble distribution derived through the measured attenuation, $dc_{\text{meas}}(\omega)$ is the sound speed anomaly derived from the displacement of the spectral peaks, and $\Delta c(\omega)$ is the difference between the two sound speed anomalies. The integration is carried out over the full measured frequency range.

Thus, the quality factor is weighted toward those frequencies most influenced by the bubbles, with a maximum value of $Q_m = 1$ for perfect agreement. For this particular example, Q_m has a value of 0.95 for the Commander and McDonald (1991) scheme, implying a close fit. We note here that if we use instead the Medwin and Breitz (1989) bubble estimation algorithm, we find $Q_m = 0.75$. This result is consistent with comparisons using other datasets and motivates our adoption of the Commander and McDonald scheme in all subsequent bubble calculations.

Low values of Q_m occur when the bubble concentration is small because the *attenuation* is difficult to measure at air fractions significantly below about 10^{-7}. However, the peak frequency displacement is still measurable at lower values and may be used for bubble inversions. At higher concentrations (in the present example at air fractions above 5×10^{-6}), peak *frequencies* become hard to measure accurately even though attenuation remains readily measurable up to air fractions of at least 6×10^{-5}, corresponding to low-frequency sound speed anomalies of -540 m s^{-1}. Thus, the applicability of the consistency check is bounded by these air-fraction limitations even though a single component of the dispersion relation is measurable over a greater range. Figure 10 is a scatterplot of Q_m showing values for air fractions spanning more than two orders of magnitude. In practice, Q_m is individually calculated for each measurement and can be used to flag values that do not satisfy a required level of consistency. A goal of our ongoing sensor development is an extension of the range over which *both* components of the dispersion relation can be accurately measured.

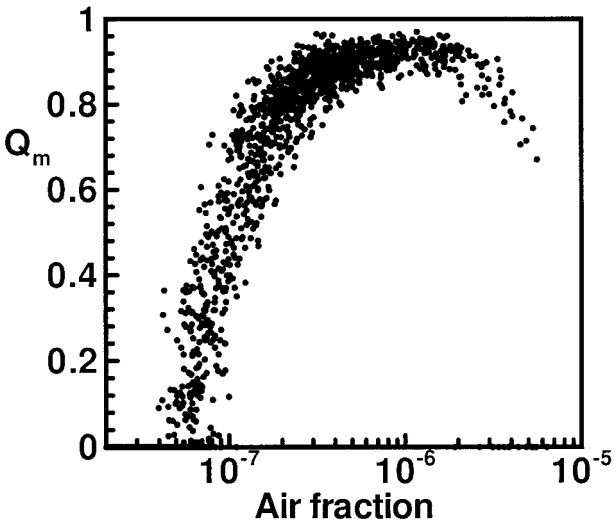

FIG. 10. Scatterplot of the measurement quality factor Q_m as a function of air fraction. Measurements may still be acquired outside the range at which Q_m is high but without the data check that comes from verifying consistency between both real and imaginary components of the dispersion relation.

Since the dispersion of sound in a bubble cloud of the kind discussed here is both linear and causal, the two components of the dispersion relation may be expected to satisfy the Kramers–Kronig relation. It has been pointed out (R. Goodman and F. Henyey 1996, personal communication) that this permits calculation of the real from the imaginary component, or vice versa, without first having to calculate the bubble population, which may have particular advantages in certain cases. As an example, for very low bubble concentrations, it may be possible to use only the more sensitive measurement of sound speed, which may then be converted to equivalent attenuation for subsequent calculation, as indicated above, thus extending the range of useful measurement.

An alternative integral check on the observations is provided by a comparison of the low-frequency sound speed given by Wood's equation (Wood 1941), which depends only on the air fraction. This equation should be applicable at frequencies appreciably below the resonant frequency of the largest bubbles contributing significantly to the air fraction, with 2.5–3 kHz usually being appropriate. Using data acquired in an experiment off the Scripps Institute of Oceanography pier, consistent comparisons were obtained between the air fraction

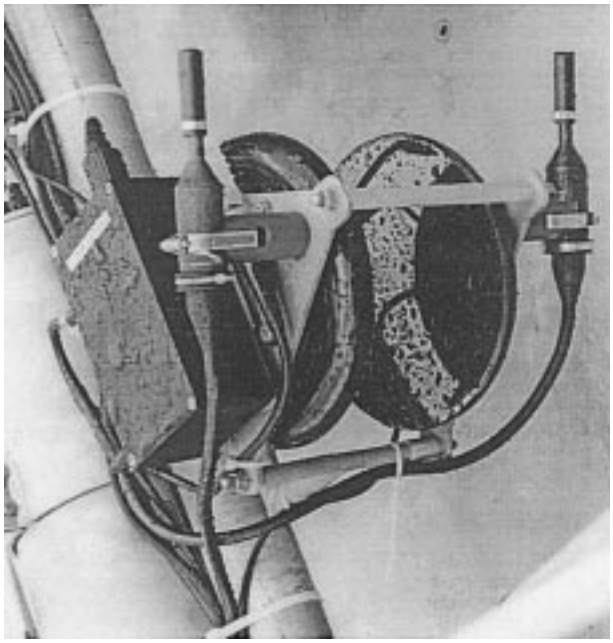

FIG. 11. Close-up of resonator attached to mooring frame. Electronics are located within the separate pressure housing shown behind the sensor head. The two small transducers on either side of the resonator are used for ambient noise and travel time measurement.

calculated from an integral over all bubble sizes measured by the resonator and the sound speed at 2.5 kHz.

7. Implementation

The two reflector plates are positioned with three spacers and cabled to a small pressure housing containing the signal generation, detection, processing, and data-logging electronics. Additional sensors have been added, including a hydrophone for ambient sound measurements, a three-axis acoustic current meter, a multiple-frequency travel time sonar, and a temperature sensor that is essential for separating the temperature contribution to sound speed from that due to the presence of bubbles. A separate recording CTD is also added to the mooring for background measurements of salinity. Comparison between the travel time sonar, resonator, and backscatter sonar measurements of bubble size distributions is discussed by Vagle and Farmer (1998). The resonator can be programmed to operate in a variety of modes, including conditional sampling in which it searches at intervals for the presence of bubble clouds and then operates according to some predetermined schedule if they are present. During normal operation it would transmit for a period of 100–1000 ms, followed by data processing and storage. The instrument is typically set to acquire successive samples repetitively at a rate of 0.5–2.0 Hz. Measurement with the travel time sonar can be alternated with the resonator or carried out simultaneously if two digital signal processors are installed.

The PVDF source covers the face of one of the reflector plates and is driven with a pseudorandom noise source formed by a 15-bit shift register. The hydrophone consists of similar PVDF covering the opposite reflector plate. Following detection, the data are digitized at 396 kHz and passed to a digital signal processor (AT&T DSP32C) that performs a preset number (typically 40) of 4096-point Fourier transforms, which are averaged. Subsequent processing includes coherent subtraction of the source signal. Peak amplitudes and frequencies are approximated by (11). The resonators are designed to operate independently or to be connected together with a common time base. Figure 11 shows a resonator sensor together with the pressure housing containing processing and data-recording electronics. The resonator dimensions and related characteristics are given in Table 1.

It should be emphasized that although the spacing between plates determines the nominal frequency of the fundamental mode, a compromise must be struck between practical dimensions and the measurement range and instrument characteristics. For given reflector plate characteristics, the aspect ratio determines the Q of the resonant peaks that increase with X/z, where X is the radius and z is the plate spacing. Higher Q leads to a more accurate measurement. However, large diameter plates are heavy and may also impede the flow if they are not oriented correctly. Representative curves derived from the theory presented above relating aspect ratio and plate characteristics to Q are shown in Fig. 12. We

TABLE 1. Instrument geometry, etc., for each individual unit.

Plate diameter	26.5 cm	37.0 cm
Plate thickness	1.27 cm	1.27 cm
Plate material	Mild steel	Mild steel
Plate spacing	15.0 cm	30.0 cm
Frequency range	~6–196 kHz	~3–196 kHz
Bubble radius range	~15–550 μm	~15–1100 μm
Number of resonant peaks	~37	~65
Typical data storage requirement	(raw) ~10 Mb h^{-1}	(raw) ~10 Mb h^{-1}
	(compressed) ~1.6 Mb h^{-1}	(compressed) ~1.6 Mb h^{-1}
Nominal disk capacity	500 Mb	500 Mb
Power consumption	0.8 A at 24 V	0.8 A at 24 V
Sampling period	0.1–1 s	0.1–1 s
Sampling frequency	0.5–2 Hz	0.5–2 Hz

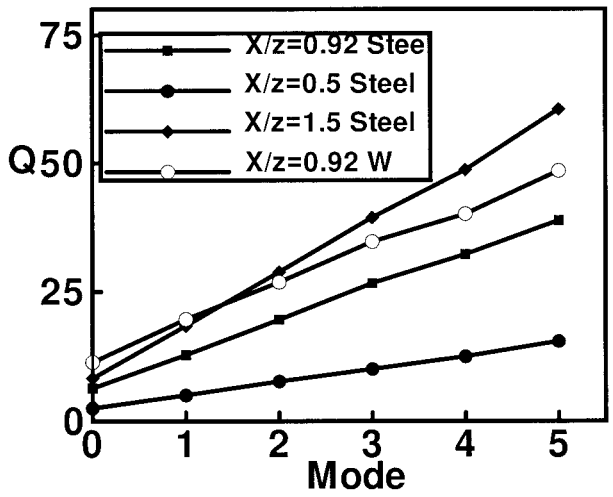

FIG. 12. Model solutions in which the resonator Q is calculated for different modes for different aspect ratios (X/z) and materials. A plate thickness of 1.27 cm is assumed. Steel plates with $X/z = 1.5$ are used in the present implementation.

have found steel plates with a ratio of $X/z = 0.92$ to be satisfactory.

Although we have developed and used a 3-kHz resonator, the parameters of which are also given in Table 1, the instruments discussed here were designed for a fundamental frequency of 6 kHz that correspond to a resonant bubble radius of 550 μm. Larger resonators can be built to detect lower-frequency signals but may be less suitable for use close to the ocean surface because of steep gradients in the bubble population.

In Fig. 13 the resonators are mounted in a frame with surface flotation. In this configuration, five resonators are set at depths from 0.7 to 5.5 m. Although each instrument has its own set of electronics, the resonators are connected by cable to a common time base (the clock on one of the resonators) and have a common power supply (the battery housing is at the bottom of the frame). The buoy is oriented into the current by a vane. Inevitably, the flotation modifies the surface flow field that must in turn affect the near-surface bubble measurements. Although we have used alternative designs in short-term measurements intended to minimize surface interactions, the configuration shown here has proved robust and convenient for longer-term deployments. The system has a hydrophone for ambient noise measurements, a CTD, an acoustic current meter, and dissolved oxygen and nitrogen (gas tension) sensors on the frame.

Operational endurance is governed by data storage and battery supply. In deployments thus far we have made little attempt to optimize data storage, as we were concerned to ensure that signal processing algorithms were optimized. However, some data compression is achieved by extracting and storing only the spectral peaks. Table 1 lists relevant data generation and storage parameters together with power requirements and battery storage. Conditional sampling contributes to the efficient use of power and data storage. In an alternative configuration for measurements in the surf zone, the instrument has been operated with a cable for power and data transfer using the Ethernet protocol.

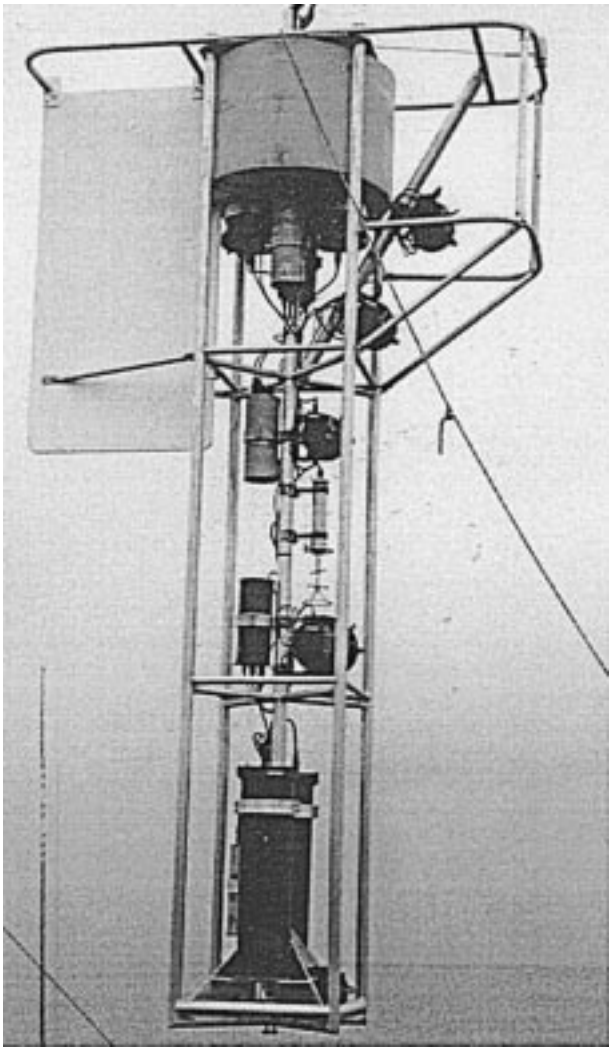

FIG. 13. Five resonators mounted on a frame for mooring in open ocean conditions. Batteries are in the pressure housing at the bottom, and polystyrene buoyancy is used for flotation. The array is 5.5 m long and includes fast-response temperature sensors, a hydrophone, a CTD probe, and a three-axis acoustic current meter.

Battery power can also be a limiting factor. In our deployments to date, power conservation has not been a primary consideration, but reduced consumption using low-power ''sleep mode'' for the processing electronics, lower-power data storage techniques, and solar power battery recharging offer considerable opportunities for improvement.

8. Representative measurements

We illustrate the type of results acquired with brief examples taken from measurements acquired in the Gulf

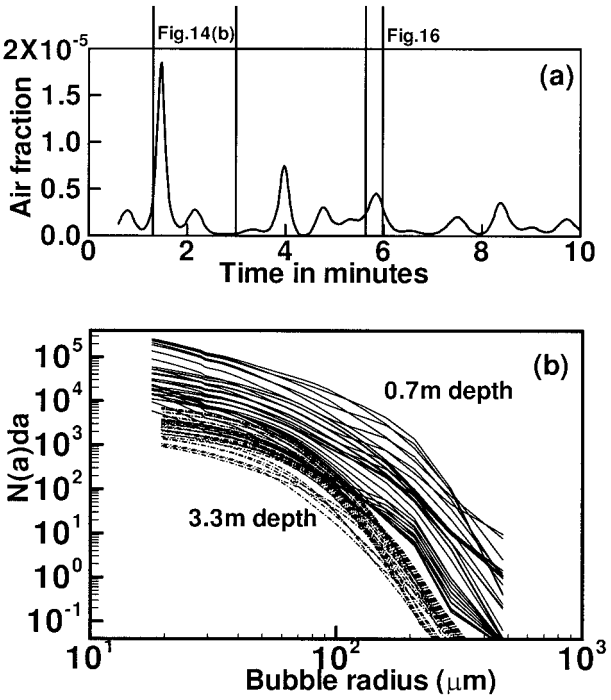

FIG. 14. (a) Time series of air fraction calculated by integration over all measured bubble sizes, showing time of datasets used in b and Fig. 16. (b) Superposition of measured bubble size distributions at depths of 0.7 and 3.3 m for the period shown in (a).

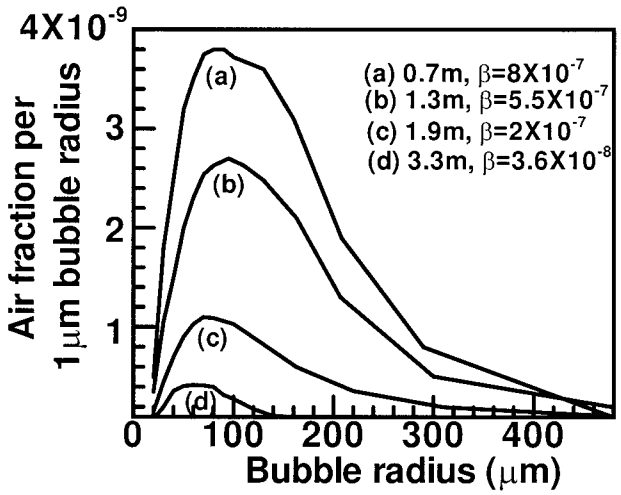

FIG. 15. Air fraction per unit (μm) radius increment $N(a)[(4/3)\pi a^3]$ for a 60-s period at four depths in the Gulf of Mexico deployment (12 Nov 1995), shown together with the total contribution to void fraction in each case. Wind speed was ~12 m s^{-1}.

of Mexico (9–19 November 1995; 28.508°N, 85.470°W) in which a set of five resonators (Fig. 13) was moored for 11 days. Wind speeds up to 14 m s^{-1} were encountered. The resonators acquired data at intervals of 1.4 s. Figure 14b shows a superposition of a short segment of bubble size distributions at depths of 0.7 and 3.3 m. Also shown (Fig. 14a) is a time series measurement of the air fraction for the same period. It is not easy to characterize the bubble size spectra in terms of a simple power-law relationship, although it is clear that for larger bubble radii, above approximately 200 μm, the concentration falls off rapidly.

The contribution to air fraction per micron radius increment (concentration times bubble volume) for a 60-s period is illustrated in Fig. 15. The curves clearly show the rapid decrease in air fraction as a function of depth (values are given in the figure). A ''dominant bubble radius'' r_{max} can be identified as the highest point on the curve that decreases slightly with increasing depth. This decrease can be expected in part because higher hydrostatic pressures result in smaller bubble radii, but there are also more subtle effects associated with gas dissolution—a changing source distribution and the local pattern of turbulence and advection.

More detailed information on the time-varying bubble size distribution at one depth is shown in Fig. 16a, where we have again displayed the results in the form of contribution to total air fraction as a function of radius, as in Fig. 15, but plotted in logarithmic form to show the very low concentrations at greater depth. This 20-s data segment emphasizes the complex structure of the bubble size distribution that can occur. For the shallowest measurement at 0.7 m, the series begins with a dominant radius r_{max} of about 80 μm, but part way through, a rapid increase in the air fraction occurs with r_{max} doubling to about 200 μm. This rapid change in dominant bubble radius with increasing air fraction does not occur at greater depths, although we note that at 1.3 m the bubble size distribution is flatter, with proportionately more of the larger bubbles than recorded at greater depths. At 1.9, 3.3, and 5.5 m, the number of bubbles decreases progressively, as expected. However, data from these deeper sensors also illustrate a slight drop in dominant bubble radius with increasing depth, similar to that shown in Fig. 15.

The rapid increase in both bubble size and air fraction recorded in the shallowest sensor suggests that an injection of near-surface water has occurred, which is possibly associated with recent wave breaking. Analysis of longer datasets shows a tendency for r_{max} to increase with higher air fractions, perhaps as a result of greater vertical velocities or turbulent diffusivities.

Figure 17 shows successive sound speed anomalies corresponding to the changing bubble size distributions of Fig. 16a. As the dominant bubble radius rises, the corresponding frequency f_{zero} of vanishing sound speed anomaly decreases from 40 to 20 kHz. If the bubbles were all of one radius, then f_{zero} would be the same as the resonant bubble frequency. In general, the frequency f_{zero} depends on contributions from the entire bubble spectrum. Nevertheless, as indicated above, the resonant frequency of a bubble of radius r_{max} is comparable to f_{zero}, and both variables may be useful for describing the most acoustically significant aspects of the bubble size distribution.

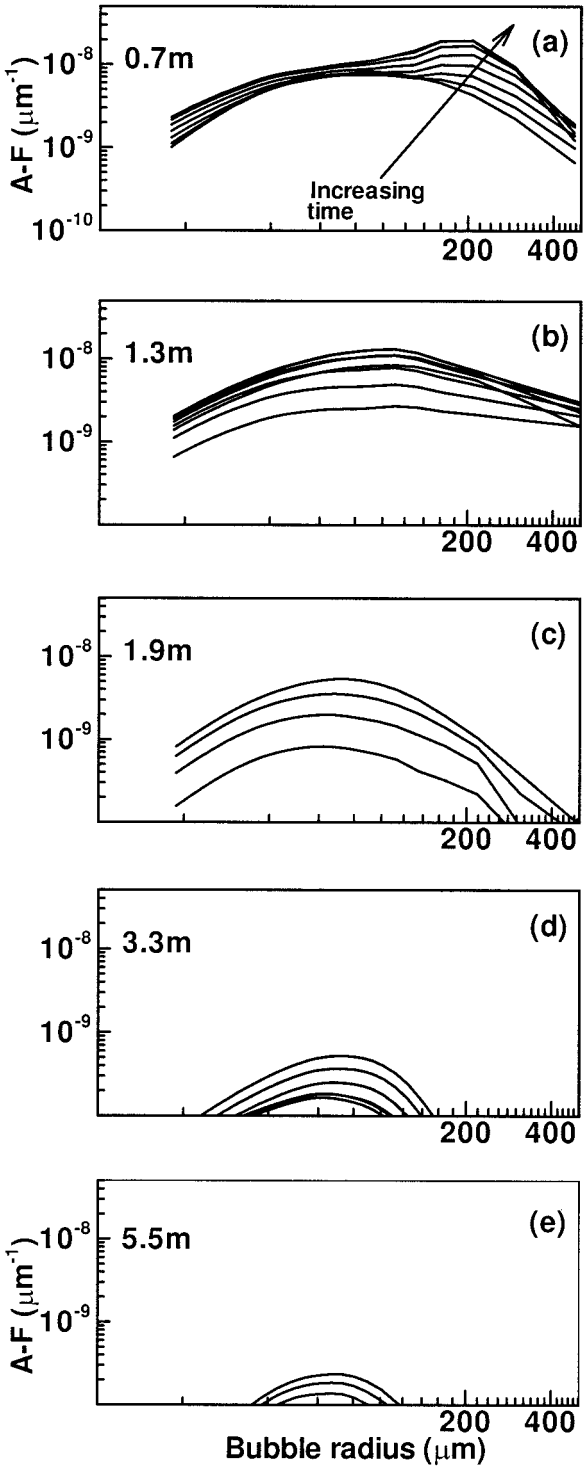

FIG. 16. (a)–(e) Bubble size distribution expressed as air fraction per unit (μm) radius increment for depths at 0.7, 1.3, 1.9, 3.3, and 5.5 m, corresponding to the period indicated in Fig. 14a, and shown on logarithmic scale so as to include results at greater depths. Successive curves correspond to increasing air fraction with time. Note shift in dominant bubble radius from ~80 to ~200 μm for the shallowest sensor. Wind speed was ~12 m s^{-1}.

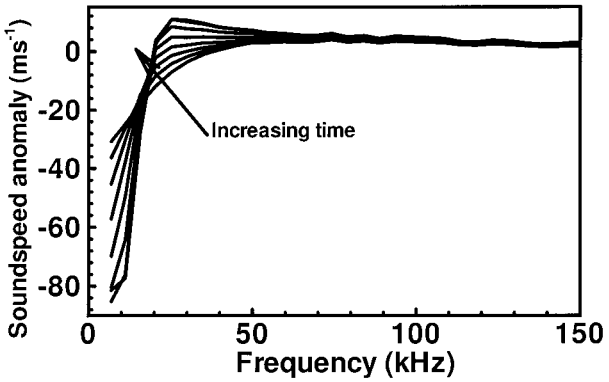

FIG. 17. Successive sound speed anomaly curves corresponding to Fig. 16a.

9. Conclusions

We have described a new implementation of the free-flooding resonator for measurement of bubble size distributions. A theoretical analysis provides the mathematical basis for describing its operation and performance. The model also leads to a definition of the appropriate Lorentzian, which is then used in the signal analysis to determine the complex acoustical dispersion of the bubble field. Following the procedure developed by Commander and McDonald (1991), bubble size distributions are computed directly from attenuation at the large number (40) of resonant peaks over the measured frequency range (6–196 kHz). However, since the sound speed is also measured, we are able to check the consistency of the results through a comparison of the two types of measurements. A data quality factor Q_m is calculated for each sample from the complex dispersion relationship.

Our implementation involves the use of identical reflector plates having PVDF transducer surfaces for both transmission and detection. In addition to simplifying the design of autonomous battery-powered instruments, the use of PVDF avoids a difficulty with air-backed Mylar employed in previous implementations since it is essentially insensitive to the rapid pressure fluctuations unavoidably encountered in the turbulent surface layer. The data are analyzed in real time with a digital signal processor. Although data analysis and storage are carried out separately for each sensor, any number of instruments can be connected together in an array having a common time base. Up to five of these instruments have been deployed in both freely drifting and moored arrays.

Natural variability in upper-ocean bubble concentrations demands rapid sampling and bubble calculation, even if the data are to be averaged over time. The instruments generate narrow spectral peaks. If the bubble distribution changes rapidly during the period of measurement, corresponding fluctuations in sound speed diffuse the average peak shape. For example, the resonator can move in and out of dense bubble clouds due to wave

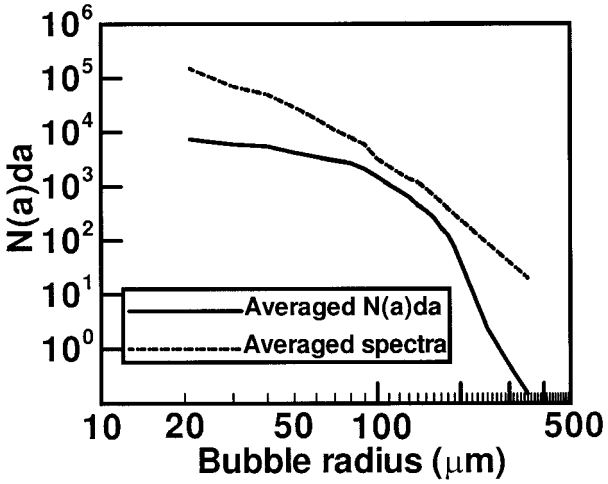

FIG. 18. Bubble size distributions inferred from averaged acoustical spectra from resonator over a 10-min period (solid line) and from averaged bubble size distributions calculated from each 300-ms sample (broken line), illustrating the serious bias that results from the former method.

orbital displacements with a period of 8–10 s. This makes the averaged peak appear broader and lower than any instantaneous value, leading to significant overestimates of the attenuation and hence overestimates of the bubble density and associated acoustic variables, such as air fraction and low-frequency sound speed. This effect is illustrated in Fig. 18, in which we have taken a 10-min time series and calculated the bubble size distribution, first by using averaged spectra (upper curve) and then by averaging the bubble distribution calculated from separate 300-ms samples (lower curve). It is apparent in this example that failure to calculate the bubble size distribution before averaging can lead to an overestimate of bubble concentrations by more than an order of magnitude, especially for the larger bubbles. Bubble calculations made at intervals of 2 s or less avoid this problem.

To assess the instrument noise level, laboratory observations were obtained in a stirred calibration tank allowed to cool through natural heat loss. Temperature was measured coherently with each resonator sample using the instrument's thermistor, which in turn was calibrated with a quartz thermometer (HP2801A). The thermistor is sampled with a resolution of 0.01°C, which is approximately equivalent to a sound speed change of 2 cm s^{-1}. The location of the mode 10 peak was calculated and compared to the temperature measurements. The steady drift in temperature was generally consistent with peak location within the resolution of temperature measurement. Time series comparisons of the peak location with the expected location based on temperature measurement showed occasional longer period deviations of up to 0.02°C (4 cm s^{-1} sound speed equivalent) together with rapid fluctuations of 0.4–2 cm s^{-1}. Deviations of this order can be expected due to the finite temperature measurement resolution (0.01°C or 2 cm s^{-1}) as well as to the effects of local gradients in the cooling tank. The stirring intensity was deliberately reduced to a low level so as to avoid bubble inclusion, and this may have led to temperature gradients sufficient to limit the accuracy of the comparison. Nevertheless, these results suggest an accuracy for this type of resonator on the of order 2 cm s^{-1}, which represents the limit of our calibration setup. Although we were unable to resolve the noise floor of the instrument, it must also be stated that other issues, such as the thermal stability of the resonator's structural materials, would have to be addressed if its full potential were to be realized. Interpretable measurements with this sensitivity and precision could hardly be expected in a bubble field, as these would require a high level of homogeneity and randomness in bubble distribution even at very low bubble concentrations. Nevertheless, the stability and precision of the basic measurement approach are reassuring.

Results acquired with the resonator in the open ocean reveal some of the complexity of real bubble fields, including changes in size distribution as a function of depth and time. In the brief but representative examples shown here it is apparent that there is a modest tendency for the radius of the dominant bubble size contributing to air fraction to decrease with increasing depth. However, this tendency can be masked by rapid fluctuations at any one depth as a function of time due to bubble injection from above. These injections might result from breaking waves or from flow instabilities in the zone of wave-enhanced turbulence near the ocean surface. In the example shown here (Fig. 16) the radius of the dominant bubble size increased from 80 to nearly 200 μm in a few tens of seconds. As discussed by Thorpe (1982), bubble size distributions depend in a subtle way on the supply from breaking waves, the turbulence and currents in the active near-surface zone, the dissolution of the primary gas constituents, and the advective effects of deeper coherent motions such as Langmuir circulation. Our results suggest the ways in which the acoustical resonator can contribute to the study of these phenomena through rapid and robust measurement of highly resolved bubble spectra.

Acknowledgments. We are grateful to Prof. H. Medwin for useful discussions in our earlier attempts at building resonators and his continued interest in our efforts to move on to an improved implementation; to Dr. K. Commander for valuable input on the bubble calculation algorithm; to Nick Hall-Patch for developing the resonator electronics; and to undergraduate co-op students Shinya Matsueda and Norman Laman as well as high school students Grant Foster and Adam Sera for their assistance in the implementation and data processing. This work received support from the U.S. Office of Naval Research.

REFERENCES

Akulichev, V. A., and V. A. Bulanov 1987: The study of sound backscattering from micro-inhomogeneities in sea water. *Progress in Underwater Acoustics,* H. M. Merklinger, Ed., Plenum, 86–92.

Blanchard, D. C., and A. H. Woodcock, 1957: Bubble formation and modification in the sea and its meteorological significance. *Tellus,* **9,** 145–158.

Booth, A. D., 1966: *Numerical Methods.* 3d. ed. Butterworth and Co., 95–96.

Breitz, N. D., and H. Medwin, 1989: Instrumentation for in-situ acoustical measurements of bubble spectra under breaking waves. *J. Acoust. Soc. Amer.,* **86,** 739–743.

Buxcey, S., J. E. McNeil, and R. H. Marks Jr., 1965: Acoustic detection of microbubbles and particulate matter near the sea surface. M.S. thesis, U.S. Naval Postgraduate School.

Commander, K. C., and R. J. McDonald, 1991: Finite-element solution of the inverse problem in bubble swarm acoustics. *J. Acoust. Soc. Amer.,* **89,** 592–597.

Duraiswami, R., 1993: Bubble density measurement using an inverse acoustic scattering technique. *ASME Cavitation and Multiphase Flow Forum,* Washington, DC, ASME, 67–74.

Fox, A. G., and T. Li, 1961: Resonant modes in a maser interferometer. *Bell System Tech. J.,* **40,** 453–488.

Green, G., 1838: Reflection and refraction of sound. *Cambridge Trans.,* **6,** 403.

Johnson, B. D., and R. C. Cooke, 1979: Bubble populations and spectra in coastal waters: A photographic approach. *J. Geophys. Res.,* **84,** 3761–3766.

Kolovayev, P. A., 1976: Investigation of the concentration and statistical size distribution of wind-produced bubbles in the near surface ocean layer. *Oceanology,* **15,** 659–661.

Lamarre, E., 1993: An experimental study of air entrainment by breaking waves. Ph.D. thesis, Woods Hole Oceanographic Institution and the Massachusetts Institute of Technology, 327 pp.

Leighton, T. G., 1994: *The Acoustic Bubble.* Academic Press, 613 pp.

——, R. J. Lingard, A. J. Walton, and J. E. Field, 1991: Acoustic bubble sizing by the combination of subharmonic emissions with an imaging frequency. *Ultrasonics,* **29,** 319–323.

——, ——, ——, and ——, 1992: Bubble sizing by the nonlinear scattering of two acoustic frequencies. *Natural Physical Sources of Underwater Sound,* B. R. Kerman, Ed., Kluwer, 453–466.

Medwin, H., 1970: In-situ acoustic measurements of bubble populations in coastal waters. *J. Geophys. Res.,* **75,** 599–611.

——, 1977a: Counting bubbles acoustically: A review. *Ultrasonics,* **15,** 7–13.

——, 1977b: Acoustical determinations of bubble-size spectra. *J. Acoust. Soc. Amer.,* **62,** 1041–1044.

——, 1977c: In-situ acoustic measurements of microbubbles at sea. *J. Geophys. Res.,* **82,** 971–976.

——, and N. D. Breitz, 1989: Ambient and transient bubble spectral densities in quiescent seas and under spilling breakers. *J. Geophys. Res.,* **94,** 12 751–12 759.

Melville, W. K., E. Terrill, and L. Ding, 1995: Field measurements of air entrainment by breaking waves. *Third International Symposium on Air–Water Gas Transfer,* B. Jähne and E. C. Monahan, Eds., AEON Verlag, 285–295.

Morse, P. M., and K. U. Ingard, 1968: *Theoretical Acoustics.* Princeton University Press, 927 pp.

Newhouse, V. L., and P. M. Shankar, 1984: Bubble size measurement using the nonlinear mixing of two frequencies. *J. Acoust. Soc. Amer.,* **75,** 1473–1477.

Phelps, A. D., and T. G. Leighton, 1996: High resolution bubble sizing through detection of the subharmonic response with a two frequency excitation technique. *J. Acoust. Soc. Amer.,* **99,** 1985–1992.

Su, M.-Y., D. Todoroff, and J. Cartmill, 1994: Laboratory comparisons of acoustical and optical sensors for microbubble measurement. *J. Atmos. Oceanic Technol.,* **11,** 170–181.

Szczucka, J., 1989: Acoustic detection of gas bubbles in the sea. *Oceanology,* **28,** 103–113.

Thorpe, S. A., 1982: On the clouds of bubbles formed by breaking waves in deep water and their role in air–sea gas transfer. *Philos. Trans. Roy. Soc. London,* **A304,** 155–210.

——, and A. Hall, 1983: The characteristics of breaking waves, bubble clouds, and near-surface currents observed using side-scan sonar. *Contin. Shelf Res.,* **1,** 353–384.

Vagle, S., and D. M. Farmer, 1992: The measurement of bubble-size distributions by acoustic backscatter. *J. Atmos. Oceanic Technol.,* **9,** 630–644.

——, and ——, 1998: A comparison of four methods for bubble size and void fraction measurements. *IEEE J. Oceanic Eng.,* in press.

Walsh, A. L., and P. J. Mulhearn, 1987: Photographic measurements of bubble populations from breaking wind waves at sea. *J. Geophys. Res.,* **92,** 14 553–14 565.

Wood, A. B., 1941: *A Textbook of Sound.* 2d ed. G. Bell & Sons, Ltd., 360.